Poincaré sections for a new three-dimensional toroidal attractor

Poincaré sections for a new three-dimensional toroidal attractor

Christophe Letellier[1] **and Robert Gilmore**[2]

[1] CORIA UMR 6614—Université de Rouen, Av de l'Université, BP 12,
F-76801 Saint-Etienne du Rouvray Cedex, France
[2] Physics Department, Drexel University, Philadelphia, PA 19104, USA

Abstract

A new 3D autonomous dynamical system proposed by Li (2008 *Phys. Lett.* A **372** 387) produces a chaotic attractor whose global topological properties are unusual. The attractor has a rotation symmetry and only a single real fixed point for the parameters used in his study. The symmetric, complex pair of fixed points cannot be ignored: they play a major role in organizing the motion on a surface of peculiar toroidal type. We describe this attractor, propose a simple, intuitive model to understand it, show that it is of toroidal type and of genus three, construct a global Poincaré surface of section with two disjoint components and use this section to locate unstable periodic orbits and determine their topological period. We also show that its image attractor is of genus one and supports flow on a simple wrinkled torus. Finally, we use the interplay between the original covering attractor and its image as an aid to understand why the Li attractor is of genus-three type.

PACS number: 05.45.−a

(Some figures in this article are in colour only in the electronic version)

1. Introduction

There are various types of chaotic dynamics. In three dimensions they have been distinguished by their global topologies, that is, the structure of the phase space that contains their chaotic attractors. Among all known chaotic attractors produced by *autonomous systems*, there are very few toroidal chaotic attractors [1], and none exhibit a symmetry. Li [2] has recently proposed a chaotic attractor whose global topology appears unusual. The dynamical system is autonomous yet the motion appears to occur on a surface with a toroidal structure. Even the most basic indices needed to identify the global topological properties, such as its genus, or the genus of its bounding torus, the nature of its global Poincaré surface of section, and the structure of its branched manifold were not known.

In the work below we describe this attractor and identify many of these topological indices. Specifically, the attractor is toroidal, it is contained within a genus-three bounding torus, and the global Poincaré surface of section has two disjoint components.

In section 2 we introduce Li's dynamical system, describe its symmetry and discuss its fixed points and their stability properties. In section 3, we describe the attractor and perform a similarity transformation in the phase space to emphasize a symmetry of the attractor. The dynamics are treated in section 4 by carefully inspecting the time evolution of the appropriate coordinates. The motion is easy to visualize as occuring on three funnels: two regular funnels that drain top to bottom and one 'anti-funnel' in which the motion is inverted, from tip to top. In order to bear some recently developed powerful tools for classifying and analyzing three-dimensional chaotic attractors, we compute the genus of the attractor in section 5. More accurately, we determine the three-dimensional manifold in $\mathbb{R}^3$ that contains the attractor, and compute the genus of its boundary, which is three. (An alternative, and more classical, derivation is given in appendix A.) This information is used to construct the global Poincaré surface of section using a simple standard algorithm in section 6. We use this Poincaré section to locate segments of a chaotic trajectory that are good approximations to unstable periodic orbits in section 7. An image attractor is constucted in section 8 by using standard methods to mod out the two-fold symmetry. The image attractor is especially useful in understanding why its double cover is of genus-three type (cf particularly figure 12). Our results are summarized in section 10.

2. The Li system

The set of three ordinary differential equations recently proposed by Li [2] is

$$\begin{cases} \dot{x} = a(y - x) + dxz \\ \dot{y} = kx + fy - xz \\ \dot{z} = cz + xy - ex^2. \end{cases} \tag{1}$$

This system of equations is invariant under the group of two-fold rotations about the symmetry axis in the phase space $\mathbb{R}^3(x, y, z)$: $R_z(\pi)$: $(x, y, z) \rightarrow (-x, -y, +z)$. It was modeled after the Lorenz system [3], but contains two additional symmetry-preserving terms: dxz in the first equation and $-ex^2$ in the third equation.

This system has three fixed points, one located on the symmetry axis at the origin $(0, 0, 0)$, and two symmetry-related fixed points. If we define x_f and z_f by

$$x_f = \sqrt{\frac{ac(k + f)}{ae + efd + kd - a}} \qquad z_f = \frac{a(k + f)}{a + fd} \tag{2}$$

the symmetric fixed points are $\left(\pm x_f, \pm x_f \times \frac{a-kd}{a+fd}, z_f\right)$.

We will study this system at two parameter values. One is the set of parameter values used by Li: $a = 40$, $c = 11/6$, $d = 0.16$, $e = 0.65$, $k = 55$ and $f = 20$. Lyapunov exponents computed by Li are $\lambda_1 = 0.23$, $\lambda_2 = 0$ and $\lambda_3 = -1.99$. These exponents lead to a Lyapunov dimension equal to 2.12. In contrast to what Li claimed [2], this attractor is in fact a limit cycle with a large period ($p = 71$). This limit cycle easily allows us to figure out the global structure of the attractor, a structure which becomes more intricated for chaotic attractors when a is increased to 41 as also investigated in this paper. Due to this, we will start our analysis with the limit cycle and then switch to the chaotic attractor. At these parameter values the symmetric fixed points are imaginary, with $x_f = 41.98i$ and $y_f = 30.32i$. The z coordinate $z_f = 69.4\dot{4}$ plays an important role in the dynamics.

The second set of parameter values involves the change $a = 40.0 \rightarrow a = 41.0$. This causes a transition from periodic behavior to chaotic behavior. The scenarios involved in such transitions have recently been described in detail in [4].

At the first set of parameter values the attractor is a limit cycle with a large period. Three projections of this periodic orbit are shown in figure 1. This cycle maps out the global topological structure of the chaotic attractor that is produced for the nearby set of parameter values at $a = 41.0$.

For both sets of parameter values the point $(0, 0, z_f)$ can be interpreted as the real image in the phase space $\mathbb{R}^3$ of the complex fixed points $(\pm x_f, \pm y_f, z_f)$. This point is as important as the real fixed point $(0, 0, 0)$.

The Jacobian for this flow is

$$
J = \begin{bmatrix} -a+dz & a & dx \\ k-z & f & -x \\ y-2ex & x & c \end{bmatrix} \xrightarrow{z\,\text{axis}} \begin{bmatrix} -a+dz & a & 0 \\ k-z & f & 0 \\ 0 & 0 & c \end{bmatrix}. \tag{3}
$$

The importance of determining the transverse stability properties along the symmetry axis has been shown in [5]. Along this axis one eigenvalue is always c and its eigenvector is along the z-axis. The other eigenvectors lie in the x–y plane. For $a = 40.0$ the transverse eigenvalues are real with opposite signs for $z < z_f$. At $z = z_f$ the positive eigenvalue vanishes. Its eigenvector is $(a, a - dz_f) = (40, 28.8\dot{8})$. The nonvanishing eigenvalue is $f - a + dz_f = -8.8\dot{8}$ and its eigenvector is $(a, f) = (40, 20)$. This eigenvector plays an important role in the dynamics.

In the range $69.4\dot{4} < z < 69.89$ the two transverse eigenvalues are negative and unequal. For z in the range $69.89 < z < 6930.11$ the eigenvalues are complex: $r \pm i\omega$, with $r = \frac{1}{2}(f - a + dz)$ and $\omega = \sqrt{z^2 - 7000z + 484375}$. The focus changes its stability from stable for $z < (a - f)/d = 125$ to unstable for $z > 125$. For $z > 6930.10$ the z-axis has the stability of an unstable node with very large positive eigenvalues.

An essential point is that the z-axis changes its stability properties from a splitting axis for $z < z_f = 69.4\dot{4}$ to a rotational axis for $z > 69.89$ [5, 6]. This can clearly be seen in the x–y projection shown in figure 1(a). For $z < z_f$ the trajectory follows a hyperbolic orbit segment as it approaches and is repelled from the z-axis. For $z > 69.89$ the trajectory spirals around the z-axis, first approaching it as z approaches $(a - f)/d$ from below, then receding as z increases above $(a - f)/d$. This behavior is clear in the x–z and the y–z projections shown in figure 1. The change in stability at $z = 125$ is indicated by the caustic in the x–y projection.

3. The attractor

The planar projections shown in figure 1 indicate that there is a second axis around which spiral motion occurs. This motion occurs around the transverse eigenvector with nonzero eigenvalue at $z = z_f$. This eigenvector is (a, f). If the x–y axes are rotated to new coordinates x'–y' through an angle $\theta = \tan^{-1}(f/a)$ and the rotated attractor is projected, the hole around this axis is more easily visible. The projections onto the rotated planes x'–z and y'–z are shown in figure 2.

It is useful to visualize the motion produced by this flow as constrained to three funnels [7]. The two symmetry-related funnels with the x' rotation axis are 'normal' funnels that we identify as **L** and **R**. Normal means that motion starts at the wide 'top' of the funnel, which is toward the outside of the projection shown in figure 2(a) near $z \simeq 50$ and $x \simeq \pm 100$ and spirals down the funnel in toward the point $(0, 0, z_f)$. Once in the neighborhood of this point it moves upward, since $c > 0$ and $z > 0$. During this phase it spirals around the z-axis for $z > z_f$. The motion here is along an 'anti-funnel' that we call **C**: it begins at the spout and
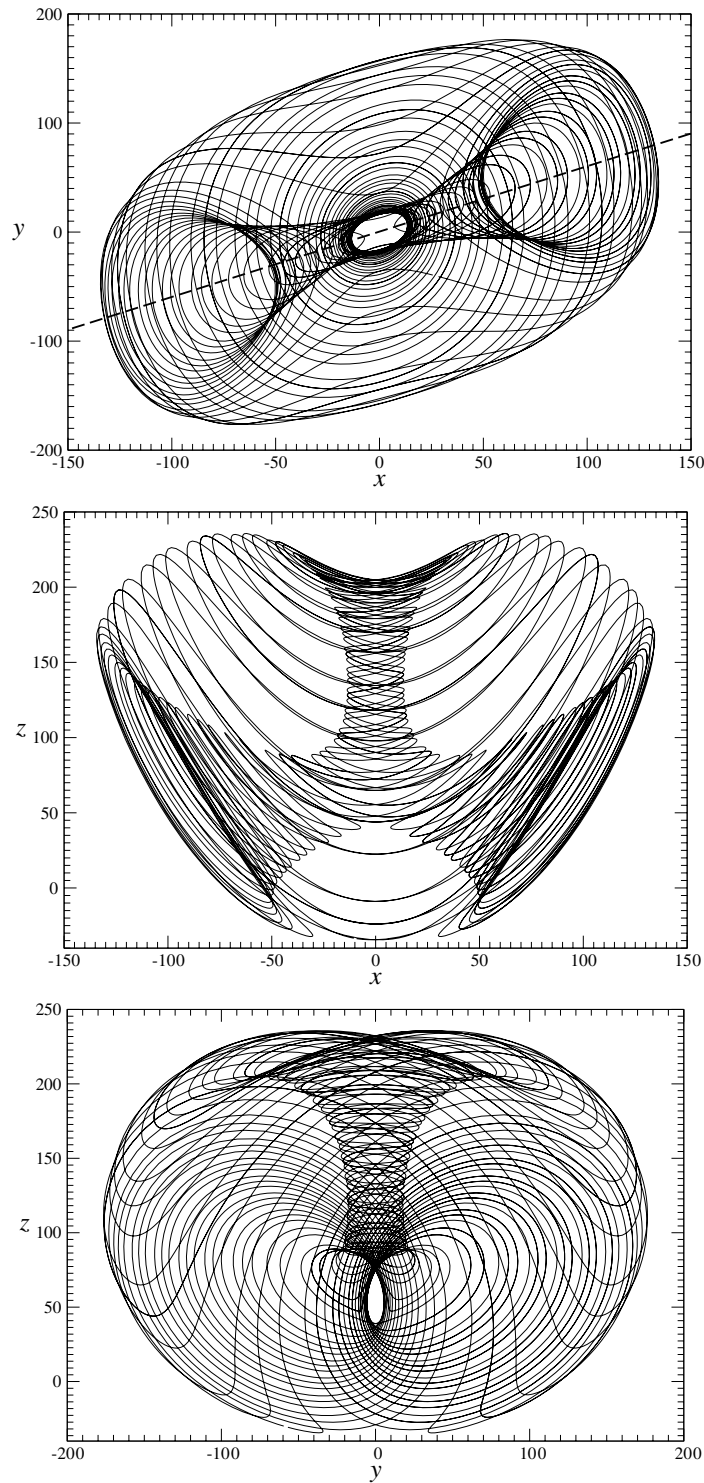
Figure 1. Limit cycle solution to system (1), projected onto three planes. Parameter values: $a = 40$, $c = 11/6$, $d = 0.16$, $e = 0.65$, $k = 55$ and $f = 20$.
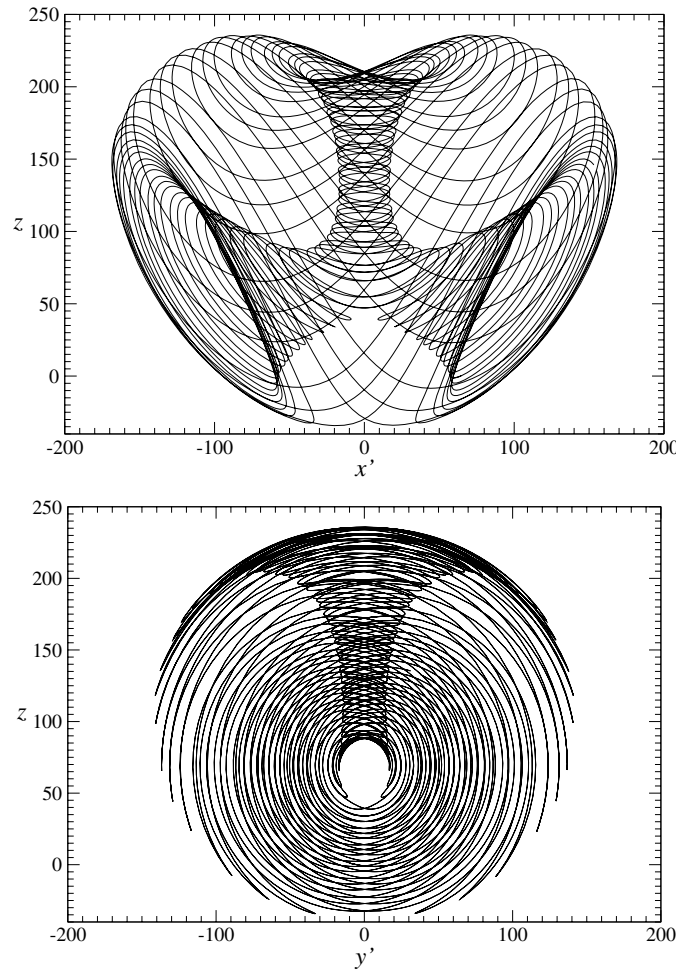
Figure 2. Projection of the limit cycle along the eigendirection of the nonzero eigenvector at $(0, 0, z_f)$ and the orthogonal direction. Rotation around the x'-axis through this point is clearly apparent. Parameter value: $a = 40.0$.

emerges at the wide end at the top of the funnel, near $z \simeq 200$. The flow then proceeds down to one of the two normal funnels **L** or **R** and begins again.

The point $(0, 0, z_f)$ is important for the dynamics because it is at the confluence of the rotation axes (funnel spouts) of the two normal funnels **L** and **R** and the anti-funnel **C**.

It is not possible to prove that this attractor is globally stable using the arguments devised by Lorenz [3]. He showed that for a large class of attractors with only linear and bilinear terms, the time derivative of $x^2 + y^2 + z^2$ is negative on the surface of a sufficiently large sphere. The demonstration fails for the Li attractor for two reasons. (1) The sum $x\dot{x} + y\dot{y} + z\dot{z}$ contains trilinear terms because of the extra terms dxz and $-ex^2$ in the Li equations that are not present in the Lorenz equations. (2) The quadratic terms in this sum are not negative definite because of the choice $c > 0$ (in the Lorenz equations the corresponding term $-bz$ has $b > 0$).

We tested boundedness as follows. The 'escape hatch' from this attractor is the positive z-axis. It is invariant: a point on this axis is ejected to $(0, 0, \infty)$. Points sufficiently near the
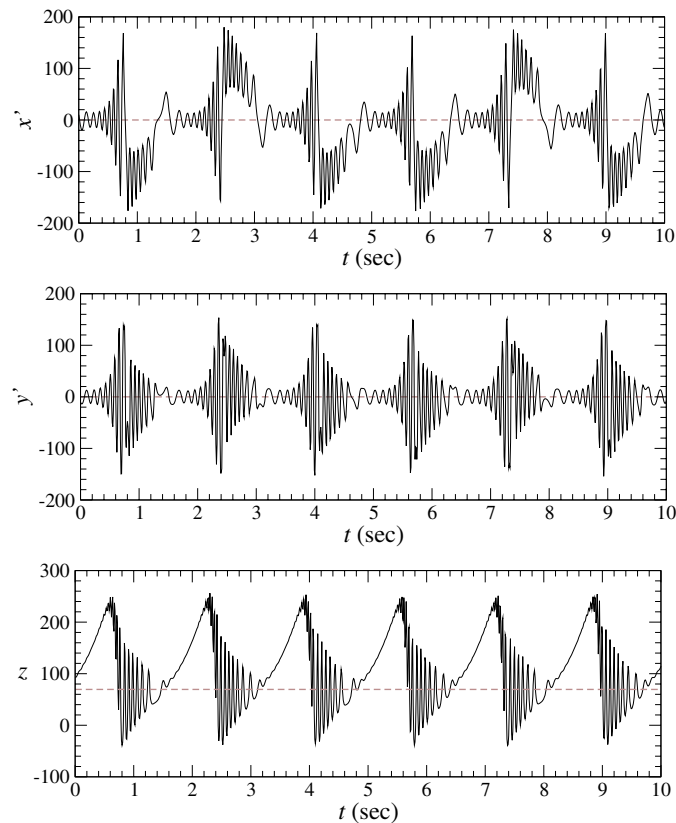
Figure 3. Plots of $x'(t)$ versus t, $y'(t)$ versus t and $z(t)$ versus t for the Li attractor. Parameter value: $a = 41.0$.

axis are also ejected to infinity. We chose a small circle of initial conditions of radius 1.0 at $z = 125$, well inside the envelope shown in figure 1(a) where the transverse stability of the z-axis changes from stable to unstable focus, and tested to see whether the motion remained bounded for long times thereafter. Evolution starting from all these initial conditions remained bounded and relaxed to the attractor outlined in this figure. Boundedness of the motion also serves to prove the existence of open neighborhoods surrounding each of the two rotation axes.

4. The dynamics

Typical time evolution $(x'(t), y'(t), z(t))$ for a point in the phase space is shown in figure 3. The evolution of the coordinate $x'(t)$ provides the most information. As the trajectory spirals up the z-axis starting at $t = 0$ the $x'(t)$ coordinate oscillates around zero and the motion is in the anti-funnel **C**. When the oscillations become extreme (amplitude in excess of about 150) the trajectory leaves the central funnel **C** and enters the funnel on the left, **L**, where $x'(t) < 0$. The trajectory remains in **L** until $x'(t)$ passes through zero ($t \simeq 1.3$) and the trajectory re-enters **C**. On leaving **L** and entering **C**, critical slowing down is observed. The signature for critical slowing down is the decrease in the oscillation frequency as the trajectory passes from **L** to **C**. As the trajectory spirals up the z-axis the oscillation frequency

increases, since $\omega = \sqrt{z^2 - 7000z + 484375}$. The imaginary critical point $(\pm x_f, \pm y_f, z_f)$ has real part $(0, 0, z_f)$, and it is in the neighborhood of this point that critical slowing down occurs.

On leaving **C** the trajectory enters either the left- (**L**, $x'(t) < 0$) or the right- (**R**, $x'(t) > 0$) hand funnel. The funnel it enters is clearly indicated by the x' coordinate: the y' and z coordinates do not provide strong signatures of the region the trajectory has entered.

The $y'(t)$ trace provides some information. In many cases just before the trajectory enters **C**, $y'(t)$ shows an avoided zero crossing. Such crossings are associated with the 'sharp turns' that can be seen inside the 'eye' in the x–y projection shown in figure 1. Critical slowing down is also observed in the $y'(t)$ trace.

The plot of $z(t)$ shows that z increases approximately linearly in time while the trajectory is in **C**, and exhibits decaying large amplitude oscillations after emerging from **C** and spiralling down the axis of either **L** or **R**.

5. Genus

A proper choice of a Poincaré surface of section is usually the key to understanding chaotic dynamics. In the present case the Poincaré section is not at all obvious. However, an algorithm exists for properly choosing a global Poincaré surface of section for low-dimensional attractors. This algorithm depends on knowing the genus of the attractor. More specifically, it depends on knowing the genus of the bounding torus that contains the attractor [8, 9]. We provide a brief review of bounding tori in appendix B.

It is clear from figures 1 and 2 that the attractor is contained within a sphere and that this sphere is penetrated by two holes, one surrounding the z-axis, the other surrounding the x'-axis. These two axes intersect at $(0, 0, z_f)$. Thus we are faced with the problem of determining the genus of a sphere that is penetrated by two intersecting holes.

This surface has genus three. We provide two arguments to demonstrate this fact. One is based on the Euler–Poincaré index theorem. This proof is given in appendix A. In this section we present a proof that also allows us to construct the global Poincaré surface of section. This proof is based on simple but elegant topological arguments.

The genus of a two-dimensional surface is unchanged by smooth deformations. At the intersection of the two holes penetrating the sphere there is a chamber. Expand this chamber until the surface is very thin, like a basketball with four holes in it, as shown in figure 4(a). Now enlarge one of the holes and deform the surface so that the remaining three holes fall inside the enlarged hole, as in the projection shown in figure 4(b). The result is a surface of genus three.

The above argument is strictly topological: it does not matter which of the four holes is stretched. In fact, our sphere surface is dressed with a flow, derived from equation (1). We have dressed each of the four holes in figure 4(a) with indicators of flow type and direction. We can transform to the canonical form for a bounding torus by choosing a particular hole around which to perform the deformation. In the canonical form the hole surrounding the regular saddle is the central hole. Thus, the hole that must be deformed is the outer rim of the central funnel **C**.

The nature of the flow in the canonical topological representation in terms of bounding tori given in figure 4(c) is as follows. When the trajectory moves upward in the anti-funnel **C** in the geometric representation (figure 1), in the canonical bounding torus representation it encircles all three holes, first moving outward toward the outer boundary, then spiralling inward until it becomes trapped in the neighborhood of either the focus (funnel) on the left or right. In the canonical representation it spirals in toward the inner boundary and then out
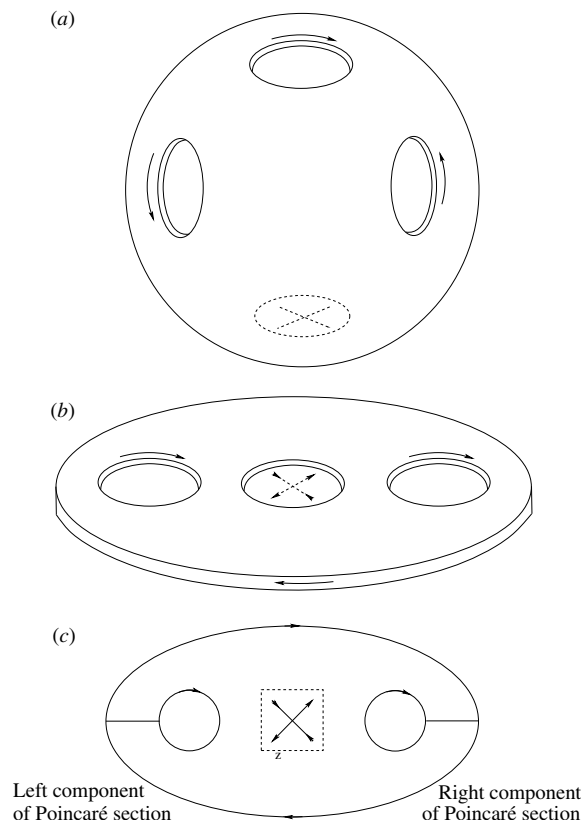
Figure 4. (*a*) The chamber at the intersection of the two intersecting holes in the sphere is expanded until the region between the inside and the outside is very thin, like the surface of a basketball. There are four holes. (*b*) Deform one of the holes so that the other three are inside in the projection shown. This surface is a torus of genus three. (*c*) Canonical form for the flow in the sphere containing two intersecting holes. The two components of the global Poincaré surface of section are shown.

again until it re-enters the anti-funnel and repeats the process. In the processes of spiralling out and in (**C**) or in and out (**L** or **R**) it maps out part of a torus.

6. Poincaré section

Since the flow exists in a bounding torus of genus three, the global Poincaré surface of section has two disconnected components. These are shown in figure 4(*c*). Working backward, it is possible to trace these two components to the corresponding components of the Poincaré surface in the original phase space $\mathbb{R}^3$. The boundary of one disc passes through the funnels **C** and **R** and closes in the upper right-hand corner of figure 2(*a*); the boundary of the other disc passes through the funnels **C** and **L** and closes in the upper left-hand corner of figure 2(*a*). As a result, none of the intersections with the two components of the Poincaré surface of section occurs with $z < 50$. The boundaries of these two components are shown schematically in figure 5. In this figure, the 'crux' links holes in figure 4(*a*).

Intersections of the chaotic attractor with the two components—the two discs delimited by red lines in figure 5—of the Poincaré section are shown in figure 6. All intersections with
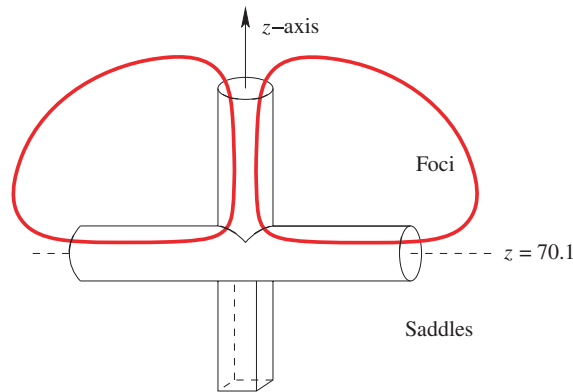
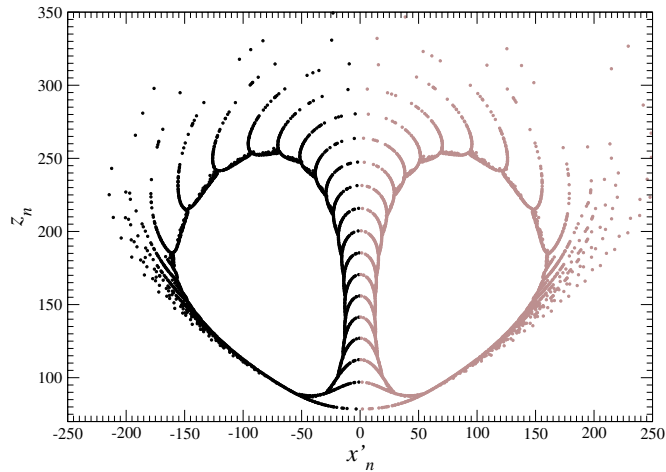**Figure 5.** Two disjoint components of the global Poincaré surface of section for the Li attractor.

Figure 6. Intersections of the chaotic Li attractor with the two components of the global Poincaré surface of section. The intersections are from opposite sides in the two half-planes $x' > 0$ and $x' < 0$. Parameter values: $(a, c, d, e, f, k) = (41, 11/6, 0.16, 0.65, 20, 55)$.

the component with $y' = 0$, $x' > 0$ have $\dot{y}' < 0$ and all intersections with the other component $y' = 0$, $x' < 0$ have $\dot{y}' > 0$.

In the transition from periodicity to chaos as a increases from 40.0 to 41.0 the trajectory occasionally explores regions very close to the z-axis. The more tightly the trajectory spirals around the z-axis in the tubular region $100 < z < 200$, the further it travels upward near the z-axis before leaving its neighborhood (for large z this axis has the transverse stability of an unstable node) and the further it progresses from the periodic set outlined in figure 2. These are the pointillist arcs that can be seen in figure 6. It is for this reason that the intersections shown in figure 6 appear to converge on the z-axis in this region ($100 < z < 200$). In fact, the trajectory never reaches the z-axis, since it is an invariant set [10]. If it did intersect the z-axis, it would extend to $z \to \infty$ and the attractor would be unstable.
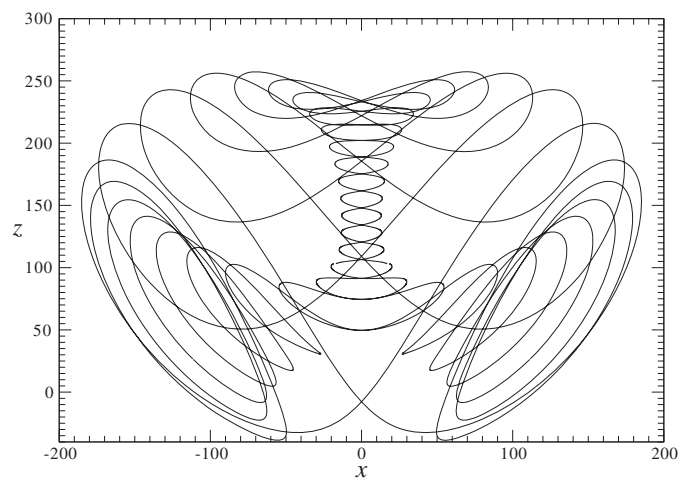
9

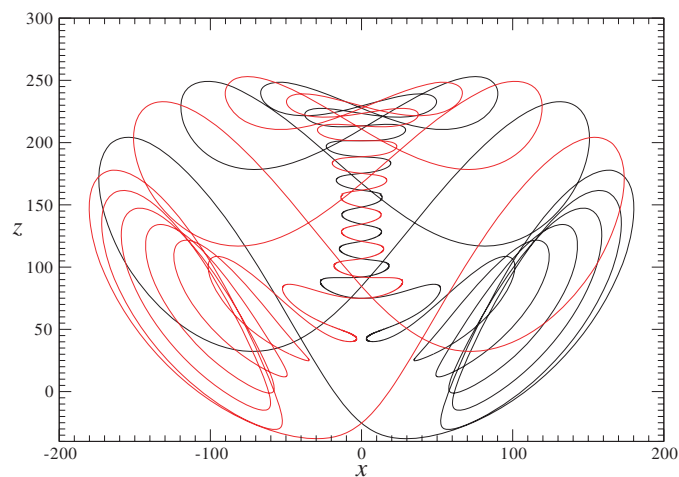**Figure 7.** A symmetric orbit of period 48.

Figure 8. A symmetric pair of asymmetric orbits of period 25.

7. Unstable periodic orbits

We used intersections with the Poincaré section to locate segments of the chaotic trajectory very close to unstable periodic orbits. These segments were located by searching for close returns in the Poincaré section. The topological period of these orbits is the number of distinct intersections with the Poincaré section.

In figure 7, we show a segment of chaotic trajectory that so closely approximates a symmetric orbit of period 48 that they cannot numerically be distinguished. In figure 8 we show a pair of asymmetric orbits of period 25. These orbits are the lowest periodic orbits which can be extracted from this chaotic attractor. This high periodicity results from the averaged winding number ($\approx$24.53) in one of the components of the Poincaré section. How these orbits contribute to the global structure of the attractor is the next step to investigate (postponed for future works).
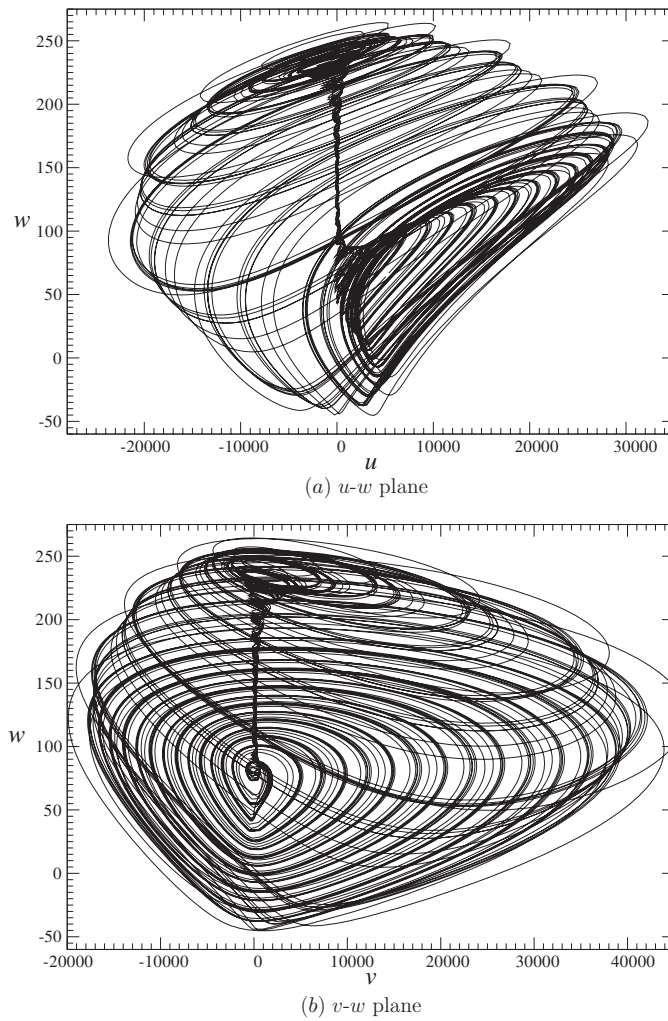
(*a*) *u-w* plane

(*b*) *v-w* plane

Figure 9. Two plane projections of the image of the Li attractor. Parameter values as for figure 6.

8. Image attractor

Experience has shown that when a dynamical system exhibits a symmetry, it is much simpler to analyze the image dynamical system than the original system [10]. Information that is determined about the image dynamical system can then be 'lifted' to the original (or 'covering') dynamical system in a relatively simple way. For this reason, the image of the Li system (1) is constructed by modding out the two-fold rotation symmetry about the *z*-axis in the usual way [10–13]. The $2 \to 1$ mapping $\Psi : \mathbb{R}^3(x', y', z) \mapsto \mathbb{R}^3(u, v, w)$ is defined by

$$\Psi \equiv \begin{vmatrix} u = \mathrm{Re}(x' + \mathrm{i}y')2 = x'2 - y'2 \\ v = \mathrm{Im}(x' + \mathrm{i}y')2 = 2x'y' \\ w = z. \end{vmatrix} \tag{4}$$

This mapping involves identifying symmetry-related pairs of points $(+x', +y', z)$ and $(-x', -y', z)$ off the symmetry axis with a single point (u, v, w) in the image space. The
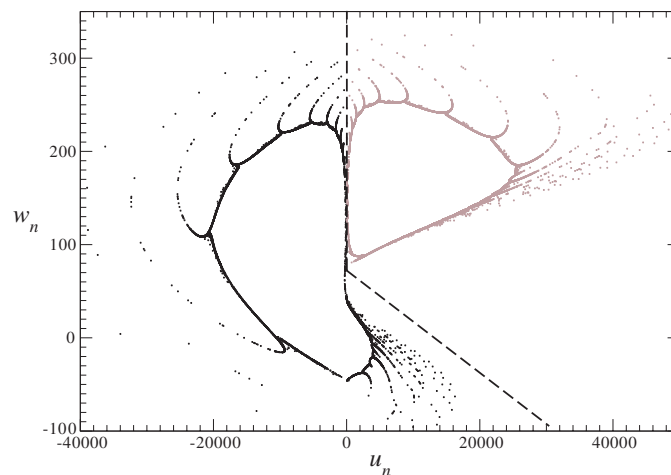
11

Figure 10. Intersections of the image attractor with the $v = 0$ plane clearly show its toroidal structure. A Poincaré section with $v = 0$, $\dot{v} < 0$ is shown to the right and above the dashed line (light color). An alternative choice for the Poincaré section ($v = 0$, $\dot{v} > 0$, (dark) is shown to the left and below the dashed line. The dashed line itself approximately follows the rotation axis, or hole, of the genus-one attractor. The break occurs around $w \approx 70$. Parameter values as in figure 6.

image phase portrait can be obtained by applying this mapping to a trajectory in the original (cover) space $\mathbb{R}^3(x', y', z)$. Two plane projections are shown in figure 9. The hole around the z-axis maps into a hole around the w-axis and the two holes around the x' half-axes, with $x' > 0$ and $x' < 0$, map into the single hole around the $u \geqslant 0$ axis. The hole appears distorted. This property has deep consequences in the structure of the original (cover) phase portrait as described below.

Since the image attractor is bounded by a genus-one torus, an appropriate Poincaré section has a single component. Figure 10 shows the intersections of the image attractor with the plane $v = 0$. The intersections outline the toroidal nature of the attractor and clearly show the folding that is a characteristic of toroidal chaos. One choice of the Poincaré section with $v_n = 0$, $\dot{v}_n < 0$ (light color) is shown to the right of the dashed line in this figure. Another possible choice, with $v_n = 0$, $\dot{v}_n > 0$ (dark color) is shown mostly on the left of the dashed line in this figure.

9. Double covers of a genus-one torus

In this section double covers of flows on a torus are investigated using the inverse of the $2 \mapsto 1$ local diffeomorphism Ψ given in equation (4). It is not necessary to lift a chaotic trajectory to visualize the global structure of the phase portrait. Simply outlining the shape of the lift of the torus is sufficient to show the shape of the double cover, which depends on the location of the rotation axis. As previously explained [10], many topologically inequivalent covers can be obtained, depending on the location of the rotation axis. The three basic cases are depicted in figure 11. When the rotation axis is in the middle of the hole of the genus-one image torus, the double cover is also a genus-one torus (figure 11(a)). When the symmetry axis is outside the image torus (figure 11(c)), there is a symmetry-related pair of genus-one tori. But when the symmetry axis does intersect the torus (figure 11(b)), the double cover is a genus-three
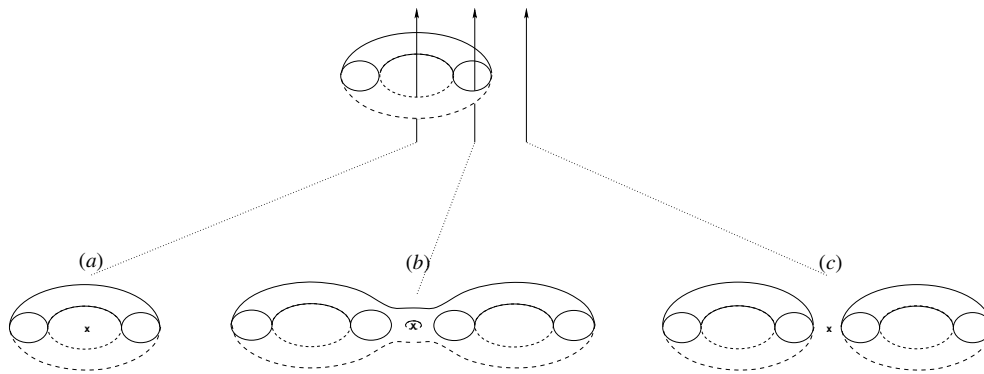
Figure 11. The three inequivalent covers of a genus-one torus depending on the location of the rotation axis. In the double covers, the rotation axis is marked by a cross.
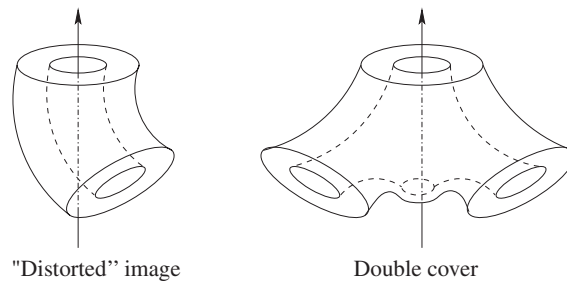

"Distorted'' image   Double cover

Figure 12. Double cover of the 'distorted' genus-one image torus. The double cover is a genus-three torus as indicated in figures 5 and 13.

torus. This is for instance what happens when the proto Lorenz attractor is lifted to its cover, the Lorenz attractor [11, 13]. It is possible to transit from one extreme case (figure 11(a)) to the other (figure 11(c)) through the so-called peeling bifurcation [10]. In previous cases, the rotation axis was always parallel to the core of the hole in the image torus. The case of the genus-three torus as a double cover was discussed starting from van der Pol toroi dal chaos considered as the image attractor [14].

None of the three covers previously described corresponds to the original Li attractor. As shown in figure 10, the rotation axis is not always parallel to the core of the hole of the genus-one torus bounding the Li attractor. In fact, the rotation axis is parallel to the core of the hole in the upper part of the attractor (figure 12) but, the lower part of the hole is distorted and the rotation axis intersects the bounding torus and the attractor it contains. The rotation axis thus crosses the torus in such a way that the upper part of the attractor is covered as in figure 11(a) and the lowest part of the attractor is covered as in figure 11(b). A cartoon of the distorted image and its double cover is shown in figure 12.

As for any cover resulting from a rotation axis intersecting the chaotic attractor, the flow of the double cover is structured around an axis with a transverse stability corresponding—at least over a significant segment—to a saddle [6]. Thus, the lowest part of the double cover of the distorted genus-one attractor is organized around a z-axis with a transverse stability of saddle type (figure 5). Since the rotation axis intersects the toroi dal surface, the double cover must be bounded by a genus-three torus.

10. Conclusion

A dynamical system recently introduced by Li exhibits a chaotic attractor with an unusual topological structure. We have studied the nature of this attractor by using several powerful, recently developed topological tools. First, we described the motion qualitatively as occurring 'on' three funnels. Next, we observed that the attractor is contained in a three-dimensional space that is topologically equivalent to a solid sphere pierced by two intersecting holes. The genus of the boundary of this surface was computed and found to be three. This already determines the nature of the global Poincaré surface of section: it consists of two disjoint components [8, 9].

In order to construct the Poincaré section, we deformed this surface to a standard canonical form for dynamical systems, that of a canonical bounding torus. In this representation the algorithm for constructing the Poincaré section was applied, and the two two-dimensional components thus determined were used to identify the two components in the original phase space. Several unstable periodic orbits were identified, along with their periods, using this Poincaré section.

The standard $2 \rightarrow 1$ local diffeomorphism was applied to this dynamical system with two-fold rotation symmetry in order to mod out the symmetry. In this way we constructed the image attractor. This attractor exists in a genus-one bounding torus and is itself of toroidal type. The lift of this image attractor back to the original double cover shows clearly why the original Li attractor exists in a genus-three bounding torus. Triple, quadruple, . . . , covers of this image are attractors with three regular funnels and one anti-funnel, four regular funnels and one anti-funnel, etc.

Appendix A

The genus g of a two-dimensional surface is defined by the Euler-Poincaré index

$$V - E + F = 2 - 2g \tag{A.1}$$

Here (V, E, F) are the number of vertices, edges and faces required to make any simplicial decomposition of the surface. This is a decomposition of the two-dimensional surface using triangles.

In figure 13 we show a decomposition of the surface containing the Li attractor using rectangular plaquets (for clarity). The conversion to a triangular decomposition is straightforward: each plaquet is divided into two parts by an edge joining two opposite vertices. This simply adds one edge and one face for each plaquet, and these additional contributions cancel in the alternating sum. For the decomposition shown for the sphere penetrated by two intersecting holes, $(V, E, F) = (32, 72, 36)$ and therefore $g = 3$.

Appendix B

It is clear just by inspection that the chaotic attractors produced by the Rossler and the Lorenz equations for their standard parameter values cannot be equivalent. No smooth deformation can deform one into the other, since the Rossler attractor is organized around one focus and the Lorenz system is organized around two. To put this another way, the phase space in which the Rossler attractor exists has one hole in it and the Lorenz attractor exists in a phase space with at least two holes in it.

This observation has been made rigorous for three-dimensional chaotic attractors [8, 9]. The attractor is 'inflated' by surrounding each point in it by a small sphere. The union
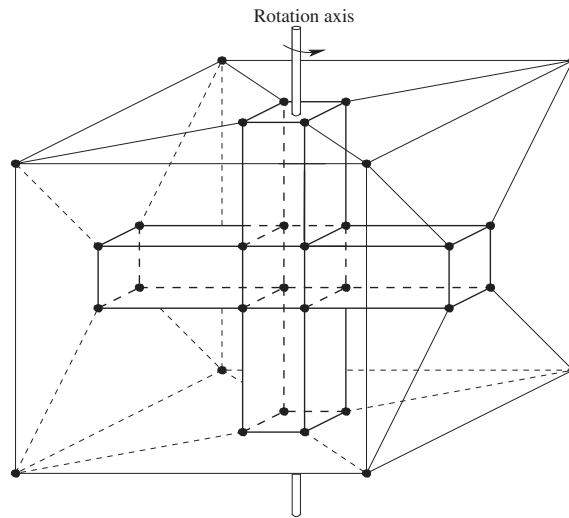
Figure 13. Surface surrounding the Li attractor has a simplicial decomposition with $(V, E, F) = (32, 72, 36)$ and thus $g = 3$.
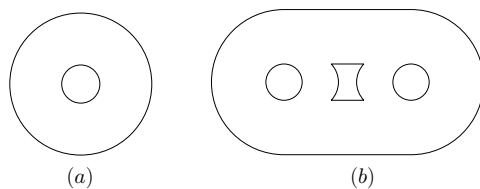

Figure 14. (*a*) Bounding torus of genus-one encloses the Rossler attractor and the image of the Li attractor. (*b*) Bounding torus of genus-three encloses both the Lorenz and the Li attractors. Round holes exclude foci and square holes exclude regular saddles.

of these spheres is a bounded three-dimensional manifold. By a standard theorem of topology, the boundary of this manifold is a two-dimensional manifold of genus g, $g = 0, 1, 2, \ldots$. Effectively, the surface is a torus with g holes in it: the sphere S^2 for $g = 0$, a regular tire tube for $g = 1$ and analogs with more holes for larger values of g. The surface associated with a chaotic attractor in this way is called its bounding torus.

The genus is determined from the flow by looking for the fixed points of the flow, when the flow is restricted to the surface. In $\mathbb{R}^3$ a flow that produces a chaotic attractor has one unstable direction, one flow direction and one stable direction, with corresponding Lyapounov exponents $\lambda_1 > 0, \lambda_2 = 0, \lambda_3 < 0$. As a result, a fixed point on the bounding torus has one stable and one unstable direction and is therefore a regular saddle. As a result, the index of each fixed point on the surface is $(-1)^{n_u} = -1$, where n_u is the number of unstable directions at the fixed point. By another theorem of topology, the sum over the indices of all fixed points on a surface is related to its genus by

$$\sum_{\text{fixed points}} (-1)^{n_u} = 2 - 2g. \tag{B.1}$$

Bounding tori of genus one and three are shown in figure 14. The Rossler attractor is contained within the surface of a genus-one bounding torus. So also is the image of the Li

attractor. The flow that generates these attractors has no fixed points on the surface. The Lorenz attractor is contained with a bounding torus of genus three. Two holes exclude the two unstable foci; the third excludes the z symmetry axis. The four singularities on this surface are associated with the z-axis, which is responsible for splitting the flow into the left- and right-hand regions, and also joining the flow from the left- and right-hand regions. Two of the four singularities are associated with the splitting directions and the other two with the joining directions. The Li attractor is also contained within a genus-three bounding torus.

Acknowledgment

References

[1]　Deng B 1994 *Int. J. Bifurcation Chaos* **4** 823
[2]　Li D 2007 *Phys. Lett.* A **372** 387
[3]　Lorenz E N 1963 *J. Atmos. Sci.* **20** 130
[4]　Letellier C, Messager V and Gilmore R 2008 *Phys. Rev.* E **77** 046203
[5]　Letellier C, Tsankov T, Byrne G and Gilmore R 2005 *Phys. Rev.* E **72** 026212
[6]　Byrne G, Gilmore R and Letellier C 2004 *Phys. Rev.* E **70** 056214
[7]　Rossler O E 1976 *Physiol. Meas.* **57** 397 (with $a = 0.343, b = 1.82, c = 9.75$)
[8]　Tsankov T D and Gilmore R 2003 *Phys. Rev. Lett.* **91** 134104
[9]　Tsankov T D and Gilmore R 2004 *Phys. Rev.* E **69** 056206
[10]　Letellier C and Gilmore R 2001 *Phys. Rev.* E **63** 16206
[11]　Miranda R and Stone E 1993 *Phys. Lett.* A **178** 105
[12]　Letellier C and Gilmore R 2007 Symmetry groups for 3D dynamical systems *J. Phys. A: Math. Theor.* **40** 5597
[13]　Gilmore R and Letellier C 2007 *The Symmetry of Chaos* (Oxford: Oxford University Press)
[14]　Letellier C, Gilmore R and Jones T 2007 *Phys. Rev.* E **76** 066204